Codoping Er-N to suppress self-compensation donors for stable *p*-type zinc oxide

Yifang Ouyang[a], Zhisen Meng[a], Xiaoming Mo[a], Hongmei Chen[a], Xiaoma Tao[a,*], Qing Peng[b,*], Yong Du[c]

[a] College of Physical Science and Technology, Guangxi University, Nanning, Guangxi 530004, People's Republic of China

[b]Department of Nuclear Engineering and Radiological Science, University of Michigan, Ann Arbor, MI48109, USA

[c] State Key Laboratory of Powder Metallurgy, Central South University, Changsha, Hunan 410083, People's Republic of China

[*] Corresponding emails: taoxiaoma@gxu.edu.cn(X.T.) qpeng.org@gmail.com (Q.P.)

Stable *p*-type doping of zinc oxide is an unsolved but critical issue for ultraviolet optoelectronic applications despite extensive investigations. Herein, we propose an Er-N codoping strategy for defect engineering of ZnO to suppress the self-compensation of the donor-type intrinsic point defects over the acceptor-type ones. Via first-principles calculations, we investigate the influence of Nitrogen and Erbium concentration on stability of the ZnO. The complex (Er_{Zn}-mN_O) consisting of multiple substitutional N on O site and one substitutional Er on Zn site is a crucial stabilizer. With an increase of the concentration of N, the absorption edges redshift to lower energy due to the impurity band broadening in the bandgap. Our results suggest that codoping Er-N into the ZnO matrix is a feasible way to manufacture stable *p*-type ZnO.

This is the author manuscript accepted for publication and has undergone full peer review but has not been through the copyediting, typesetting, pagination and proofreading process, which may lead to differences between this version and the Version of Record. Please cite this article as doi: 10.1002/adts.201800133.

Stable p-type ZnO is important but challenge to achieve despite extensive efforts with single dopants or codopants. First-principles study reveals that the Er-N codopant is stable, suppressing the self-compensation of the donor-type intrinsic point defects, with a strong infrared absorption when the N concentration is above 1.389%. The absorption edges redshift when N concentration increases.

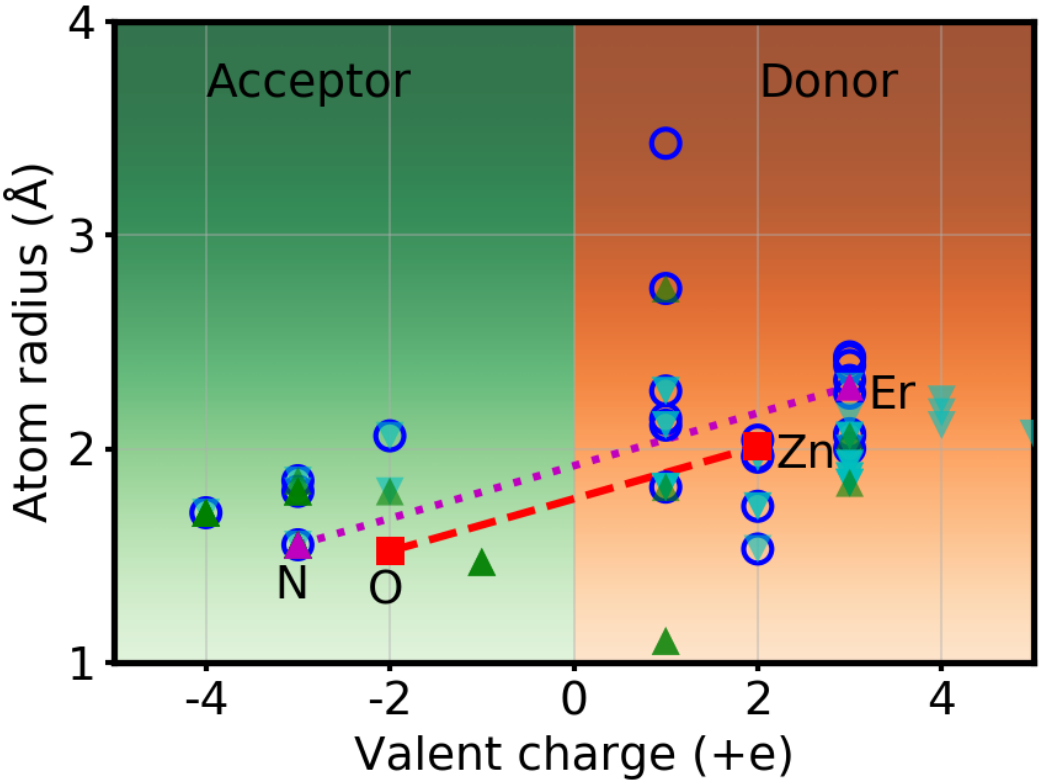

Keywords: p-type ZnO; Er-N codoping; first principles; defect formation energy;

Novelty and Impact: The Er-N codopant is stable for ZnO, suppressing the self-compensation of the donor-type intrinsic point defects, with a strong infrared absorption when the N concentration is above 1.389%.

Zinc oxide (ZnO) is one of the most important semiconductors with attractive properties [1-3] and wide applications [4]. However, some vital problems that hinder the further development of ZnO-based optoelectronic devices still remain unsolved; for example, *p*-type dopping ZnO with high hole concentration is still unavailable, partially due to the strong self-compensation of the donor-type intrinsic point defects (IPDs) over the acceptors in ZnO itself. Therefore, suppressing the self-compensation and improve the solubility of the acceptors is critical to produce stable and reliable *p*-type ZnO, which becomes a highly elevated task and is required by fabrication of different kinds of semiconductor devices. Till now, many doping strategies have been proposed in order to realize *p*-type ZnO. Some groups reported doping strategies by doping Group I or V elements (Li, Na, Ag, N, P, As, etc.) to the ZnO matrix to produce *p*-type ZnO [5-10]. These methods were simple, but the as-produced *p*-type ZnO was not stable due to the strong self-compensation and low solubility of the acceptors. For this reason, Yamamoto and Katayama-Yoshida proposed a strategy by codoping N and Al(Ga) into ZnO to decrease the Madelung energy and ionization energy, and thus enhance the incorporation of the N acceptors [11]. Besides, some theoretical and experimental codoping methods by using N and many other different dopants was also carried out to produce *p*-type ZnO, for example, N codoping with P [12], Mg [13], Ag [14, 15], Li [16-19], B [20, 21], Be [22], and As [23], etc. Other codoping methods, such as Li-F [24], Al-As [25] and Ag-S [26, 27], Mg-F [28], Li-P [29], were proposed as well.

Indeed, doping (including codoping) is a simple and effective means to improve the electrical and optical properties of ZnO [30-33]. Except for the Group I, III and/or V elements mentioned above, rare earth (RE)-doped ZnO materials also show great potential for producing optoelectronic devices due to their unique electronic structures. Extensive studies have been carried out for RE-doped ZnO, including Eu [32], Er [33, 34], Tm [35], Yb [36], La [37] and Nd [38]. Among them, Er is a very promising dopant because the unique intra-4*f* transitions of Er can produce strong 1.54 μm ($^4I_{13/2}\rightarrow{}^4I_{15/2}$) emission [39], which lies in the

minimum loss region of silica-based optical fibers and can be used in future optical telecommunication. Er can inherently inhibit the donor-type IPDs in ZnO and favor the formation of acceptor-type IPDs [31]. However, doping Er into the ZnO lattice alone is not likely to form *p*-type ZnO with high hole concentration due to the low concentration and solubility of the acceptors.

In this paper, a codoping strategy by codoping Er and N into ZnO is proposed to surpass the difficulties as noted above. We study via first-principles calculations the crystal structures, formation energies, ionization energies, band structures and optical properties of the Er-N codoped ZnO. We find the Er_{Zn}-mN_O complexes were the main configurations in the Er-N codoped ZnO systems due to their small lattice distortions, formation energies and ionization energies. Electronic and optical properties of these systems were further analyzed.

Results

Structures. The view of the part of the configurations of the codopant models considered are illustrated in Figure 1(a). Crystal parameters of the Er-N codoping ZnO:($n\mathrm{Er_{Zn}}$-$m\mathrm{N_O}$) systems were computed with the condition that all the degrees of freedom of the system are free to move. The results of the lattice constants and volumes of these configurations are shown in Figure 1(c) and (d). From the results of ZnO:($\mathrm{Er_{Zn}}$-$m\mathrm{N_O}$) (m=0, 1, 2, 3, 4) in Figure 1(c), it can be found that with increasing the doping concentration of N c_N, lattice parameter a firstly increases a little but decreases when c_N>1.389 at.%. The lattice parameter c firstly decreases, then increases as c_N>1.389 at.%, and decreases again when c_N>2.778 at.%. For ZnO:($n\mathrm{Er_{Zn}}$-$\mathrm{N_O}$) (n=0, 1, 2, 3, 4), parameter c behaves similarly as that of ZnO:($\mathrm{Er_{Zn}}$-$m\mathrm{N_O}$), but parameter a is very different because it increases monotonically with increasing the Er concentration. Figure 1(d) shows the change of the cell volume as a

function of the doping concentration. The cell volume only decreases slightly with increasing the N concentration. On the contrary, the cell volume increases dramatically with increasing the Er concentration. This could be understood from the fact that the ionic radius of Er^{3+} (0.890 Å) is much bigger than that of Zn^{2+} (0.740 Å), leading to volume expansion for Er doping [33]. Therefore, the doping N influences much less on the crystal parameters than that of doping Er in the Er-N codoping systems.

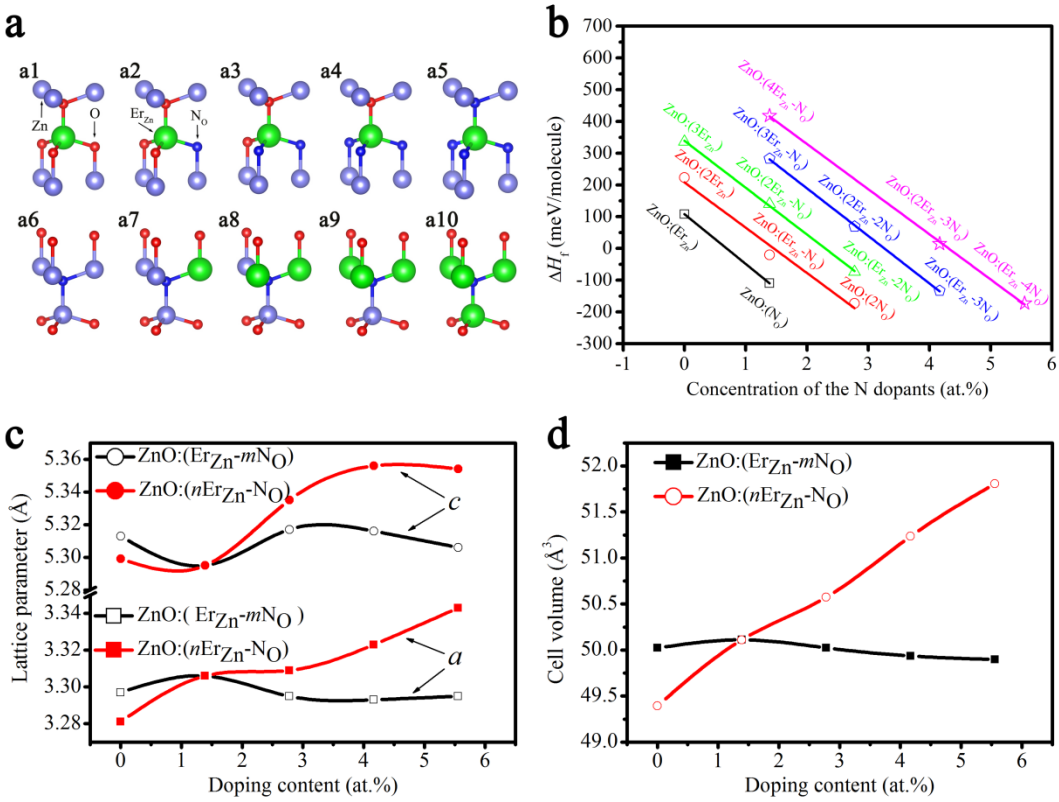

Figure 1. Er-N co-dopants. a Partial view of the models considered: (a1-a5) ZnO:(Er_{Zn}-mN_O) (m=0, 1, 2, 3, 4) and (a6-a10) ZnO:(nEr_{Zn}-N_O) (n=0, 1, 2, 3, 4). (a2) and (a7) are actually the same model observed from different angles. **b** Formation enthalpies of per molecule of ZnO:(Er_{Zn}) for different co-doping concentration, the line for guide to variation of N and Er with co-doping concentration. For some total co-doping concentration, the formation enthalpy is lower when the more N dopant. **c** Lattice parameters (a and c) for hexagonal structures and **d** cell volume for the configurations co-doped as a function of the Er and N doping concentrations. The lattice constants and cell volume decrease slightly with N doping concentration, while increase with Er doping concentration. The N doping

influences much less on the crystal parameters than that of Er doping in the Er-N co-doping systems.

Formation enthalpies. The effect of concentration of Er-N codoping on the formation enthalpies was presented in Figure 1(b). The formation enthalpies vary linearly with the concentration of N for the complexes with same number of total dopants. Two representative codoping complexes [ZnO:(Er_{Zn}-mN_O) (m=0, 1, 2, 3, 4) and ZnO:(nEr_{Zn}-N_O) (n=0, 1, 2, 3, 4)] were used and the corresponds to concentration of the N (Er) dopants of 0, 1.389, 2.778, 4.167, and 5.556 at.% for different m (n), respectively.

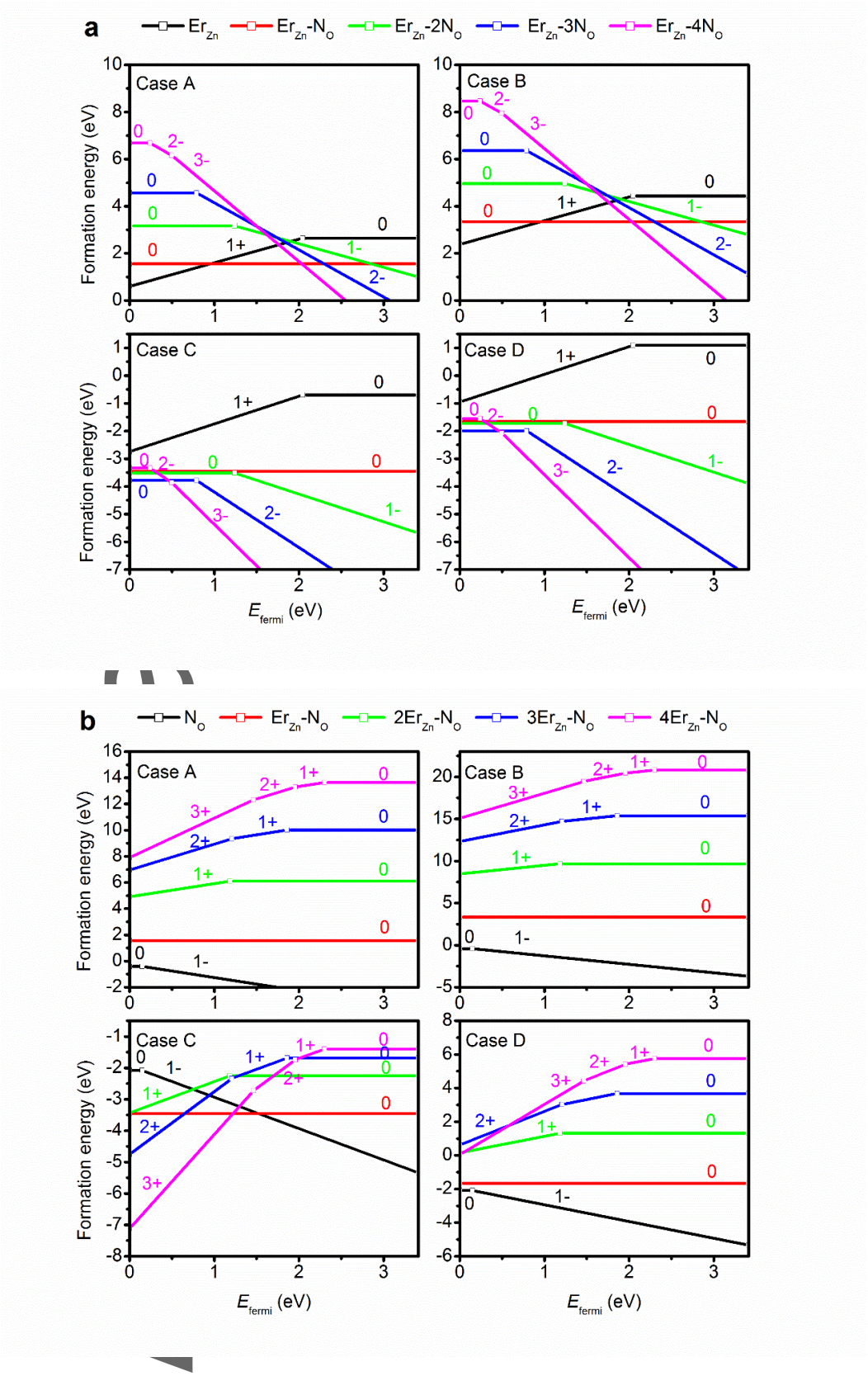

Figure 2 Formation energy versus Fermi level of doping systems for different extreme chemical potential conditions (case A: Zn-rich, Er-rich, case B: Zn-rich Er-poor, case C: Zn-poor, Er-poor, case D: Zn-poor, Er-rich). **a** Formation energies of ZnO:(Er_{Zn}-mN_O) (m=0, 1, 2, 3, 4) as a function of the Fermi level for different chemical potential conditions. **b** Formation energies of ZnO:(nEr_{Zn}-N_O) (n=0, 1, 2, 3, 4) as a function of the Fermi level for different chemical potential conditions. The defect transition energies became shallower with increasing the N concentration and the nEr_{Zn}-N_O complexes are not as stable as the Er_{Zn}-mN_O complexes.

Ionization energy and defect formation energy. Ionization energies of the defects with different N doping concentration (Figure 4) show that the values of ε(0/-1) for Er_{Zn}-$3N_O$ and Er_{Zn}-$4N_O$ complexes are 1.008 and 0.244 eV respectively, while the values of ε(-1/-2) for Er_{Zn}-$3N_O$ and Er_{Zn}-$4N_O$ complexes are 0.574 and 0.233 eV, respectively. The values of ε(0/-1) are greater than those of ε(-1/-2) for the Er_{Zn}-$3N_O$ and Er_{Zn}-$4N_O$ complexes, indicating that the defect charge is directly transformed from neutral to -2. The defect formation energies of ZnO:(Er_{Zn}-mN_O) (m=0, 1, 2, 3, 4) and ZnO:(nEr_{Zn}-N_O) (n=0, 1, 2, 3, 4) are displayed in Figure 2 as a function of the Fermi level under different chemical potential conditions. The range of the Fermi energy is given by the calculated VBM (0 eV) and CBM (3.412 eV). The defect transition energies became shallower with increasing the N concentration. Under Zn-rich growth conditions, the formation energy increases as the N concentration grows, with the neutral Er_{Zn}-N_O complex approaching the lowest formation energy. However, under the Zn-poor growth environment, the formation energy of the neutral Er_{Zn}-$4N_O$ complex is the highest, and it can be reduced to minimum after the ionization to -3.

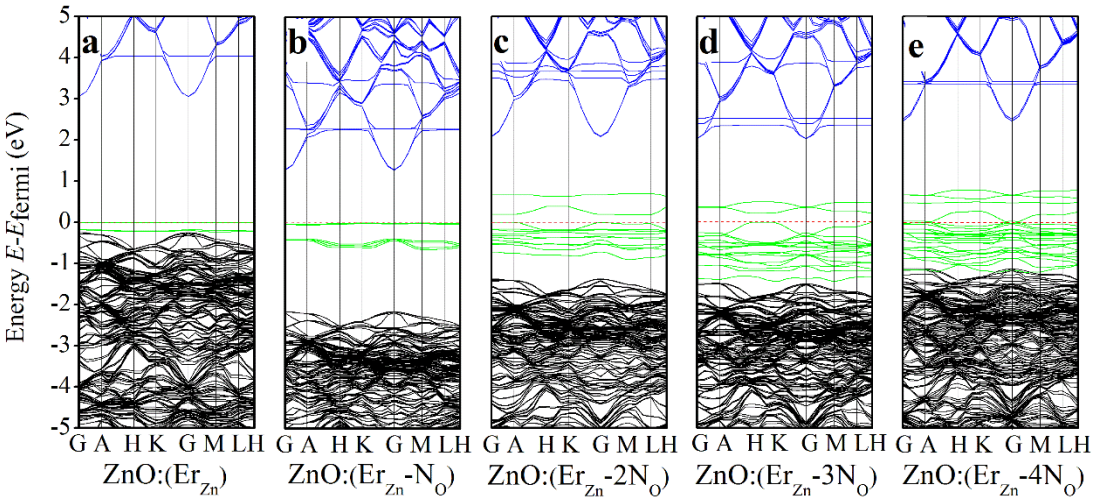

Figure 3. Band structures of ZnO:(Er$_{Zn}$-mN$_O$) (m=0, 1, 2, 3, 4) calculated by GGA+U method. The Fermi level is set to zero. An obvious impurity band (green lines) is introduced in the band gap after N atoms are doped into the ZnO:(Er$_{Zn}$) matrix. With increasing the N concentration, the impurity band gradually expands and finally becomes tail of the valence band.

Electronic properties. The band structures of the ZnO:(Er$_{Zn}$-mN$_O$) (m=0, 1, 2, 3, 4) doping systems were calculated referring to the Fermi level at zero, as shown in Figure 3. Their corresponding VBM, CBM and E_g (summarized in Table S2 in the Supplementary Information) show that both the VBM and CBM move toward lower energy when N is doped into the ZnO:(Er$_{Zn}$) system. With increasing the N concentration, nevertheless, both the VBM and CBM move toward higher energy. The band gap E_g also increases with an increase of N atoms in the ZnO:(Er$_{Zn}$) system, as E_g=3.281, 3.432, 3.470, 3.507, and 3.565 eV, for m=0, 1, 2, 3, and 4, respectively. Of them, the result of E_g=3.281 at m=0 agrees well with the available experimental value of 3.23 eV [40]. Noticeable impurity bands (green lines) are introduced in the band gap after N atoms are doped into the ZnO:(Er$_{Zn}$) matrix. With increasing the N concentration, the impurity band gradually expands and finally becomes tail

of the valence band. The band-tail states are not good extended states for carriers, thus leading to degradation of the electrical properties of the ZnO:(Er_{Zn}) as a semiconductor.

The total and partial density of states (DOS) of electrons in the ZnO:(Er_{Zn}-mN_O) (m=0, 1, 2, 3, 4) systems (Figure S3 in Supplement Information) manifest that the valence band is composed of the hybridization among the Zn-3*d*, O-2*p* and Er-4*f* states, and the VBM is mainly attributed to the O-2*p* states. The conduction band is hybridized by the Zn-4*s*, Er-5*p* and Er-4*f* states, and dominated by Zn-4*s* states. After doping N into the ZnO:(Er_{Zn}) matrix, the Er-4*f* states move to lower energy. The resonance bonding effect of the Zn-3*d* states may weaken the hybridiztion between the O-2*p* and Zn-3*d* states, thus leading the valence band toward the lower energy. On the other hand, the shift of Zn-4*s*, Er-5*p* and Er-4*f* states to the lower energy leads to the downward shift of the CBM. In addition, it can be seen that the impurity band introduced by doping N is originated by the N-2*p* states. With further increasing the N concentration, the hybridization between N-2*p* and Zn-3*d* states and the localization of Er-4*f* states are gradually enhanced, but the hybridization between Er-4*f* and Zn-3*d* states weakens, which may be the reason for the VBM moving to higher energy.

Discussion

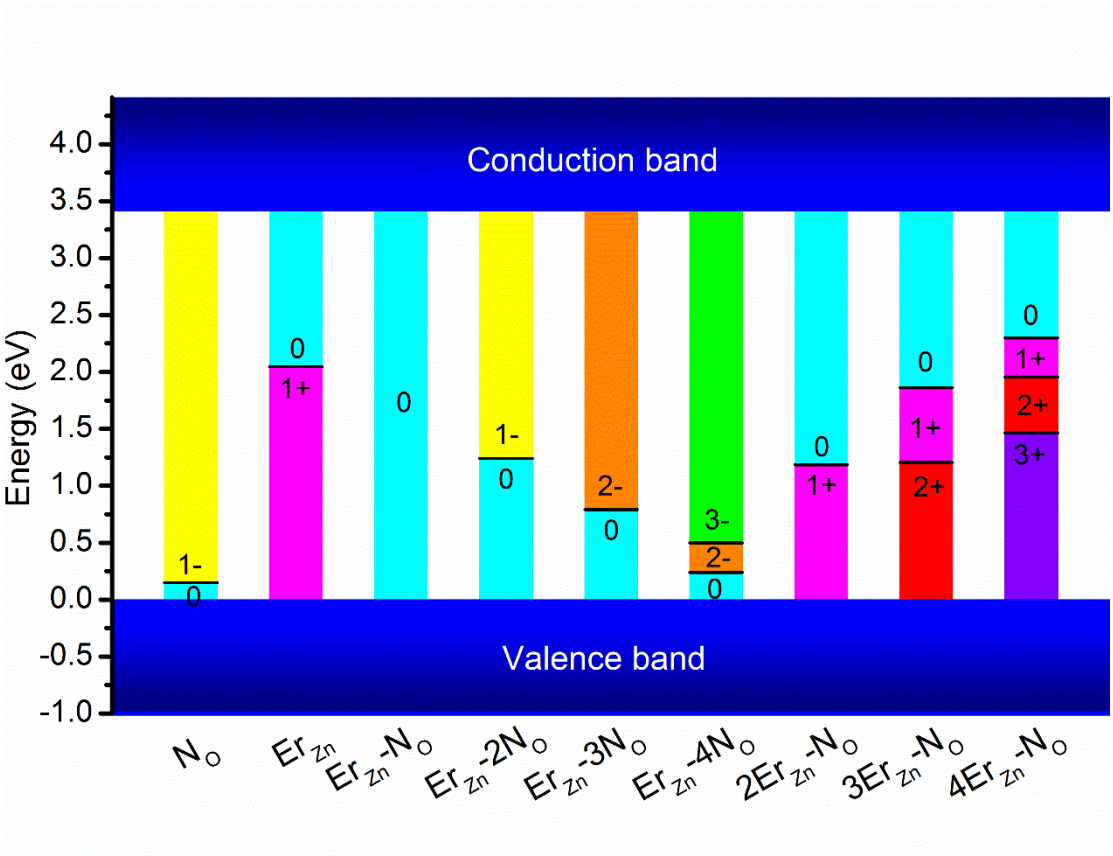

Figure 4. Ionization energies equivalent to the point symbol in Figure 2, alongside the relevant charge states. The ionization energies of $n\mathrm{Er_{Zn}}$-$\mathrm{N_O}$ complexes are deeper than those of the $\mathrm{Er_{Zn}}$-$m\mathrm{N_O}$ complexes.

The defect ionization energies of $\mathrm{Er_{Zn}}$-$m\mathrm{N_O}$ (m=0, 1, 2, 3, 4) gradually become smaller with increasing the N concentration, which means that the defect ionization energies can be reduced significantly when more N atoms are incorporated into the $\mathrm{Er_{Zn}}$-$\mathrm{N_O}$ complex, thus leading to stable p-type doping of ZnO. Figure 4 show that the ionization energy of ZnO:($\mathrm{Er_{Zn}}$-$4\mathrm{N_O}$) is the lowest in Er-N codoping syetems. This means that ZnO:($\mathrm{Er_{Zn}}$-$4\mathrm{N_O}$) is

more likely to ionize and reduce the resistivity. Therefore, how to improve the concentration of the Er_{Zn}-$4N_O$ complex in ZnO:(Er_{Zn}-mN_O) systems under the Zn-poor and Er-rich environment is the key to realize excellent *p*-type ZnO films. On the other hand, under Zn-poor conditions, the presence of Zn vacancy will enhance the *p*-type conductivity because it will introduce more holes in the valence band [41].

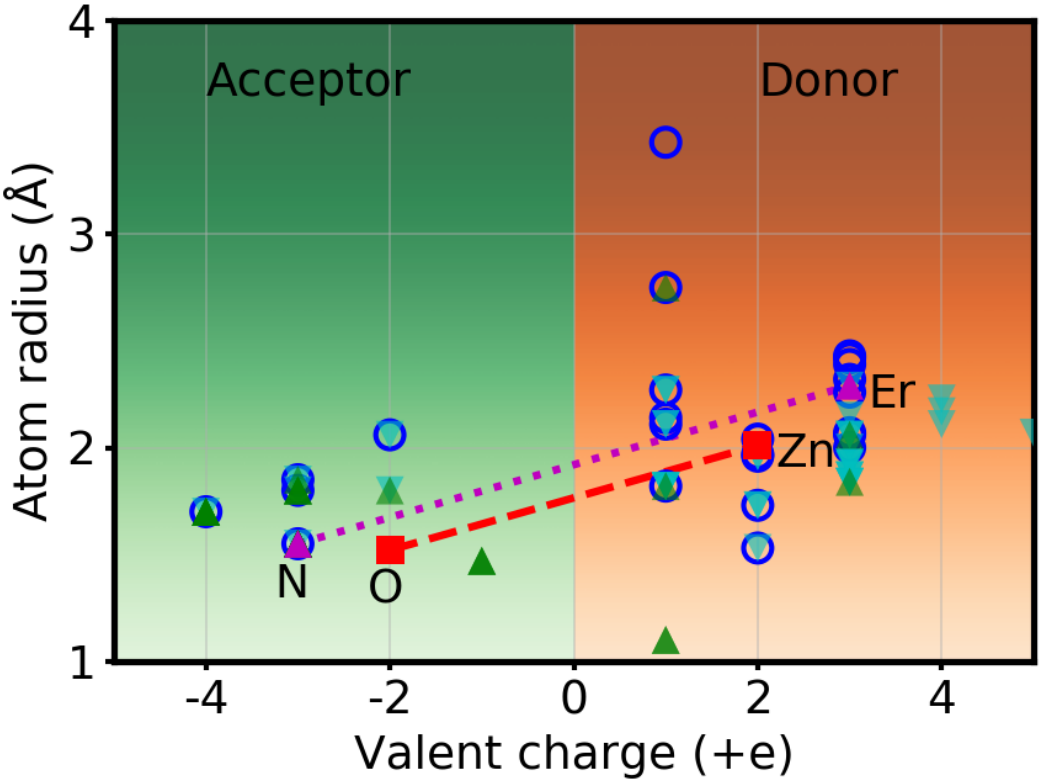

Figure 5 Chart of dopants. Both single dopant and codopants for *p*-type ZnO reported in ~100 literature are summarized according to their valent charge and atom radius from periodic element table. The matrix elements Zn and O (red squares) are for reference, compared to Er and N (Magenta triangles) in this study. The element doping and codoping are displayed by circle and filled triangles respectively.

The *p*-type of ZnO doping and codoping elements from previous published literature have been summarized in the "Chart of dopants" according to their valent charge and atom radius (Figure 5). It can be seen from the figure 5 that the marks of Er and N are closer to the positions of O and Zn, and they fall on the positions of dopsnts that have been implemented. This also indicates that Er-N co-doped ZnO may be feasible experimentally. The doping mechanism of dopants in Figure 5 was analyzed based on the available experimental data and theoretical model [4]. For example, group-I doping introduced shallow acceptor state. As for the group V *p*-type doping, the mechanism is complicated and is different for different element. Most studies focus on the N-doped ZnO. The drawback of N-doping is the quite limited solubility of N. Which leads to low hole concetrations and high resistivities. The other things is that besides the formation of N_O acceptors, the shallow double donors $(N_2)_O$ could be developed and resulted in the *p*-type conduction unstable [42]. The Er-N codoping extends the solubility of N in ZnO and improves the stability of *p*-type ZnO.

Conclusion

In summary, structural, electronic and optical properties of the ZnO:($n\mathrm{Er_{Zn}}$-$m\mathrm{N_O}$) systems in terms of crystal structures, formation energies, ionization energies, and band structures have been studied systematically by the first-principles method. The obtained results show that the N concentration less influences the crystal structures than that of Er. The ionization energies of ZnO:($\mathrm{Er_{Zn}}$-$m\mathrm{N_O}$) complexes are shallower than those of ZnO:($n\mathrm{Er_{Zn}}$-$\mathrm{N_O}$), which makes the $\mathrm{Er_{Zn}}$-$m\mathrm{N_O}$ complexes the main configurations in Er-N codoped ZnO systems. When more N atoms are doped to be combined with $\mathrm{Er_{Zn}}$ to form larger $\mathrm{Er_{Zn}}$-$m\mathrm{N_O}$ complexes, the defect ionization energies can be reduced and favor to form stable *p*-type ZnO:($\mathrm{Er_{Zn}}$-$m\mathrm{N_O}$) films. The ionization energy of ZnO:($\mathrm{Er_{Zn}}$-$4\mathrm{N_O}$) is the lowest in Er-N codoping syetems, and it can realize *p*-type semiconductor material with excellent

performance. Our results show that codoping Er-N into the ZnO matrix may be a feasible way to realize stable *p*-type ZnO.

Method

First-principles calculations

The exchange-correlation potentials of electron-electron interactions were approximated by the generalized gradient approximation (GGA) with Perdew-Burke-Ernzerhof (PBE) functionals. The interactions between the ion core and its valence electrons were described by ultra-soft pseudopotentials. The configurations of the valence electrons used in the calculations were Zn ($3d^{10}$ $4s^2$), Er ($4f^{12}$ $5s^2$ $5p^6$ $6s^2$), O ($2s^2$ sp^4), and N ($2s^2p^3$). GGA+U method was used to optimize the system energies to correct the bandgap value of ZnO, where the $U_{p,O}$, $U_{d,Zn}$, and $U_{f,Er}$ values adopted in this work were 7, 10.5 and 6 eV, respectively. The reciprocal space was sampled by a 4×4×3 Monkhorst-Pack mesh in the irreducible Brillouin zone for the 3×3×2 supercell. The cutoff energy for the plane wave basis was set to be 510 eV. In the optimization process, the energy variation, maximum tolerances of the force, stress, and atomic displacement were set to be 1.0×10^{-6} eV/atom, 0.03 eV/Å, 0.05 GPa and 0.01 Å, respectively. More details about the model and computations are in the Supplementary Information.

Acknowledgments

This work was financially supported by the National Natural Science Foundation of China Grant Nos. 11464001, 11504060 and 51661003, the Scientific Research Project for Higher Education of Guangxi Zhuang Autonomous Region (Grant No. KY2015ZD006), and the Doctoral Scientific Research Foundation of Guangxi University (Grant No. XBZ160084).

References

[1] A. Tsukazaki, A. Ohtomo, T. Onuma, M. Ohtani, T. Makino, M. Sumiya, K. Ohtani, S. F. Chichibu, S. Fuke, Y. Segawa, H. Ohno, H. Koinuma, M. Kawasaki, *Nat. Mater.* **2005**, *4*, 42-46.

[2] Z. R. Tian , J. A. Voigt, J. Liu, B. McKenzie, M. J. McDermott, M. A. Rodriguez, *Nat. Mater.* **2003**, *2*, 821-826.

[3] P. Sharma, A. Gupta, K. V. Rao, F. J. Owens, R. Sharma, R. Ahuja, J. M. Guillen, B. Johansson, G. A. Gehring, *Nat. Mater.* **2003**, *2*, 673-677.

[4] F. Xiu, J. Xu, P. C. Joshi, C. A. Bridges, M. P. Paranthaman, *Springer* **2016**, *218*, 105-140.

[5] M. L. Tu, Y. K. Su, C. Y. Ma, *J. Appl. Phys.* **2006**, *100*, 2208.

[6] Y. J. Zeng, Z. Z. Ye, W. Z. Xu, D. Y. Li, J. G. Lu, L. P. Zhu, B. H. Zhao, *Appl. Phys. Lett.* **2006**, *88*, 3270.

[7] A. Allenic, W. Guo, Y. B. Chen, M. B. Katz, G. Y. Zhao, Y. Che, Z. D. Hu, B. Liu, S. B. Zhang, X. Q. Pan, *Adv. Mater.* **2010***, 19*, 3333-3337.

[8] S. S. Lin, J. G. Lu, Z. Z. Ye, H. P. He, X. Q. Gu, L. X. Chen, J. Y. Huang, B. H. Zhao, *Solid State Commun.* **2008**, *148*, 25-28.

[9] S. P. Wang, C. X. Shan, B. H. Li, J. Y. Zhang, B. Yao, D. Z. Shen, X. W. Fan, *J. Cryst. Growth*. **2009**, *311*, 3577-3580.

[10] M. A. Myers, J. H. Lee, Z. Bi, H. Wang, *J. Phys.: Condens. Matter*. **2012**, *24*, 145802.

[11] T. Yamamoto, H. Katayamayoshida, *Jpn. J. Appl. Phys.* **2014**, *38*, L166-L169.

[12] Y. R. Sui, B. Yao, L. Xiao, L. L. Yang, J. Cao, X. F. Li, G. Z. Xing, J. H. Lang, X. Y. Li, S. Q. Lv, *Appl. Surf. Sci.* **2013**, *287*, 484-489.

[13] L. Chen, Z. Xiong, Q. Wan, D. Li, *Opt. Mater.* **2010**, *32*, 1216-1222.

[14] D. Li, W. Zhang, X. Yu, Z. Jiang, L. Luan, Y. Chen, D. Li, *Appl. Surf. Sci.* **2012**, *258*, 10064-10067.

[15] W. Li, C. Kong, G. Qin, H. Ruan, L. Fang, *J. Alloys Comp.* **2014**, *609*, 173-177.

[16] Y. Gai, G. Tang, J. Li, *J. Phys. Chem. Solids* **2011**, *72*, 725-729.

[17] T. P. Rao, M. C. S. Kumar, *J. Alloys Comp.* **2011**, *509*, 8676-8682.

[18] H. Shen, C. X. Shan, J. S. Liu, B. H. Li, Z. Z. Zhang, D. Z. Shen, *Phys. Status Solidi* **2013**, *250*, 2102-2105.

[19] C. X. Shan, J. S. Liu, Y. J. Lu, B. H. Li, F. C. Ling, D. Z. Shen, *Opt. Lett.* **2015**, *40*, 3041-3044.

[20] Y. R. Sui, B. Yao, Z. Hua, G. Z. Xing, X. M. Huang, T. Yang, L. L. Gao, T. T. Zhao, H. L. Pan, H. Zhu, *J. Phys. D Appl. Phys.* **2010**, *42*, 065101.

[21] Z. Xiong, L. Chen, C. Zheng, L. Luo, Q. Wan, *Scripta Mater.* **2010**, *63*, 1069-1072.

[22] X. Tang, Y. Deng, D. Wagner, L. Yu, H. Lü, *Solid State Commun.* **2012**, *152*, 1-4.

[23] E. Przezdziecka, E. Kaminska, K. P. Korona, E. Dynowska, W. Dobrowolski, R. Jakiela, L. Klopotowski, J. Kossut, *Semicond. Sci. Tech.* **2007**, *22*, 10.

[24] L. Cao, L. Zhu, Y. Li, M. Yang, Z. Ye, *Mater. Lett.* **2012**, *86*, 34-37.

[25] L. Balakrishnan, S. Gowrishankar, J. Elanchezhiyan, N. Gopalakrishnan, *Physica B* **2011**, *406*, 4447-4452.
[26] N. X. Tian, L. Xiang, L. Zhong, Y. C. Yong, H. S. Cheng, Z. W. Hui, *Appl. Surf. Sci.* **2014**, *316*, 62-65.
[27] Y. Xu, T. Yang, B. Yao, Y. F. Li, Z. H. Ding, J. C. Li, H. Z. Wang, Z. Z. Zhang, L. G. Zhang, H. F. Zhao, *Ceram. Int.* **2014**, *40*, 2161-2167.
[28] G. Muruganandam, N. Mala, S. Pandiarajan, N. Srinivasan, R. Ramya, E. Sindhuja, K. Ravichandran, *J. Mater. Sci. Mater. Electr.* **2017**, *28*, 18228-18235.
[29] P. Sharma, R. Bhardwaj, A. Kumar, S. Mukherjee, *J. Phys. D Appl. Phys.* **2018,** *51***,** 015103.
[30] B. Y. Oh, M. C. Jeong, T. H. Moon, W. Lee, J. M. Myoung, J. Y. Hwang, D. S. Seo, *J. Appl. Phys.* **2006**, *99*, 1348-1419.
[31] P. K. Nayak, J. Yang, J. Kim, S. Chung, J. Jeong, C. Lee, Y. Hong, *J. Phys. D Appl. Phys.* **2008**, *42*, 035102.
[32] X. Zeng, A. Junlin Yuan, L. Zhang, *J.phys.chem.C* **2008**, *112*, 3503-3508.
[33] Z. Meng, X. Mo, X. Cheng, Y. Zhou, X. Tao, Y. Ouyang, *Mater. Res. Expr.* **2017**, *4*, 035903.
[34] Y. Yang, Y. Li, C. Wang, C. Zhu, C. Lv, X. Ma, D. Yang, *Adv. Opt. Mater.* **2014**, *2*, 240-244. [35] Y. Liu, C. Xu, Q. Yang, *J. Appl. Phys.* **2009**, *105*, 198.
[36] X. Yu, S. Liang, Z. Sun, Y. Duan, Y. Qin, L. Duan, H. Xia, P. Zhao, D. Li, *Opt. Commun.* **2014**, *313*, 90-93.
[37] X. L. Xu, Y. Chen, S. Y. Ma, W. Q. Li, Y. Z. Mao, *Sen. Actu. B Chem.* **2015**, *213*, 222-233.
[38] H. Li, Y. Lv, J. Li, Y. Ke, *J. Alloys Comp.* **2014**, *617*, 102-107.
[39] M. Lluscà, J. López-Vidrier, A. Antony, S. Hernández, B. Garrido, J. Bertomeu, *Thin Solid Films* **2014**, *562*, 456-461.
[40] S. D. Senol, *J. Mater. Sci.: Mater. Electr.* **2016**, *27*, 7767.
[41] M. A. Lahmer, K. Guergouri, *Mater. Sci. Semicond. Proc.* **2015**, *39*, 148-155.
[42] J. L. Lyons, A. Janotti, d. W. Van, Chris G, *Appl. Phys. Lett.* **2009**, *95*, 252105.

Supplementary Information

Codoping Er-N to suppress self-compensation donors for stable *p*-type zinc oxide

Yifang Ouyang[1], Zhisen Meng[1], Xiaoming Mo[1], Hongmei Chen[1], and Xiaoma Tao[1,*], Qing Peng[2,*], Yong Du[3]

[1] College of Physical Science and Technology, Guangxi University, Nanning, Guangxi 530004, People's Republic of China

[2] Department of Nuclear Engineering and Radiological Science, University of Michigan, Ann Arbor, MI48109, USA

[3] State Key Laboratory of Powder Metallurgy, Central South University, Changsha, Hunan 410083, People's Republic of China

[*] Corresponding emails: taoxiaoma@gxu.edu.cn(X.T.) qpeng.org@gmail.com (Q.P.)

1. Formation Energy

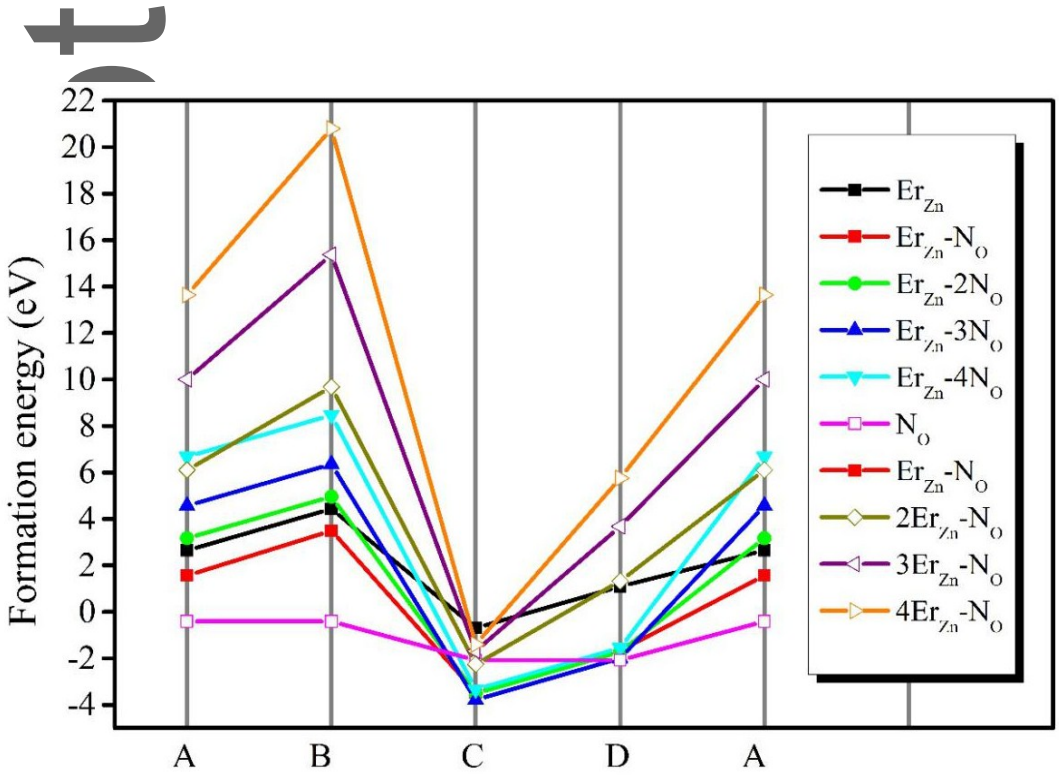

Figure S1. Effect of Chemical potential on the charge-neutral formation energies of doping systems for different extreme chemical potential conditions (case A: Zn-rich, Er-rich, case B: Zn-rich Er-poor, case C: Zn-poor, Er-poor, case D: Zn-poor, Er-rich). The formation energies under Zn-poor and Er-rich are the lowest for all the complexes, indicative of the easiest way of successfully codoping Er and N into the ZnO matrix under this condition.

Figure S1 shows charge-neutral formation energies with different dopants under the four extreme chemical potential conditions. The charge-neutral formation energies of ZnO:(Er_{Zn}-$m$$N_O$) ($m$=0, 1, 2, 3, 4) complexes are lower than those of ZnO:($n$$Er_{Zn}$-$N_O$) ($n$=0, 1, 2, 3, 4) complexes, indicating that N atoms are easier to substitute the O atoms to form the Er_{Zn}-$m$$N_O$ defect complexes with Er_{Zn} under the four extreme conditions. Besides, for all of the above doping complexes, growing under the Zn-poor conditions results in significantly lower formation energies than those under the Zn-rich environment, which indicates that Zn-poor crystal growth environment is more favorable for the doping process. Li et al. [S1] also found

that the formation energy of Er doped ZnO under Zn-poor growth condition was lower than that of Zn-rich growth condition. The formation energies under Zn-poor and Er-rich are the lowest for all the complexes, indicative of the easiest way of successfully codoping Er and N into the ZnO matrix under this condition.

2. Relative chemical potentials.

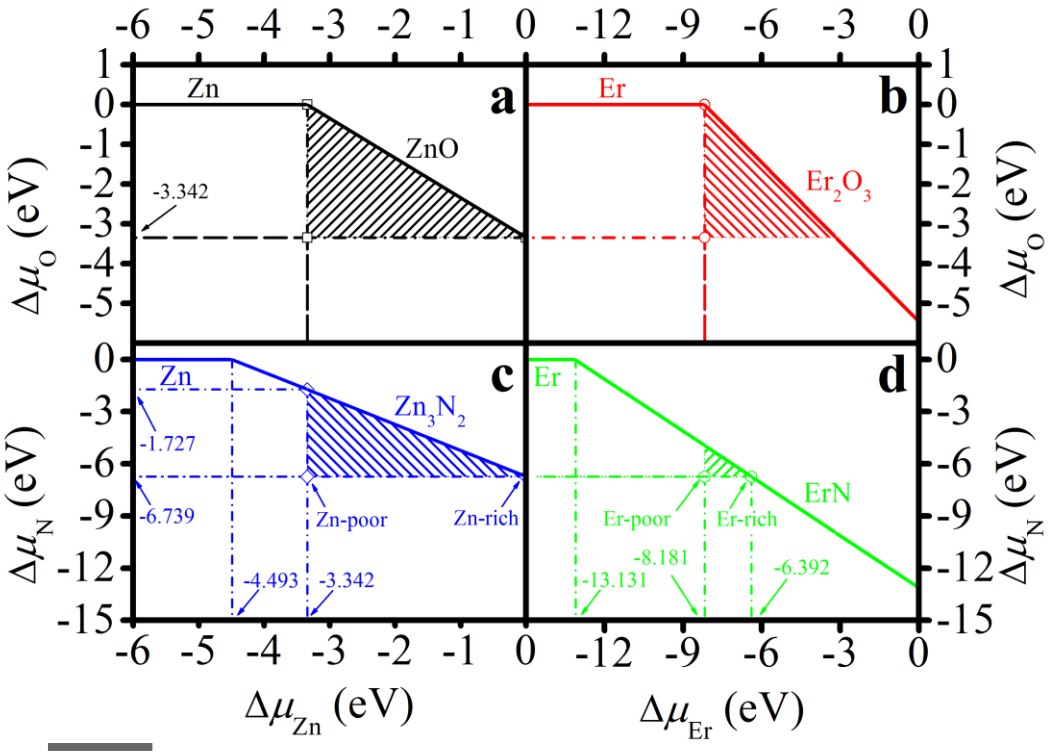

Figure S2. Relative chemical potentials $\Delta\mu_i$ (i=Zn, Er and N) by the constraint of $\Delta\mu_O$. For the doping in ZnO, four extreme conditions can be obtained from $\Delta\mu_{Zn}$, $\Delta\mu_{Er}$ and $\Delta\mu_N$ by the constraint of $\Delta\mu_O$.

Table S1. Extreme growth conditions obtained from Figure S2 by the constraint of $\Delta\mu_O$.

Constraint	$\Delta\mu_{Zn}$	$\Delta\mu_{Er}$	$\Delta\mu_O$	$\Delta\mu_N$

Zn-rich, Er-rich	0	-6.392	-3.342	-6.739
Zn-rich, Er-poor	0	-8.181	-3.342	-6.739
Zn-poor, Er-rich	-3.342	-6.392	0	-1.727
Zn-poor, Er-poor	-3.342	-8.181	0	-1.727

In order to avoid the appearance of elementary substance (Zn, O_2, Er, and N_2), the $\Delta\mu_i$ (i=Zn, O, Er, or N) should satisfy the four conditions: $\Delta\mu_{Zn}\leq 0$ eV, $\Delta\mu_O\leq 0$ eV, $\Delta\mu_{Er}\leq 0$ eV, and $\Delta\mu_N\leq 0$ eV. Meanwhile, in order to avoid the formation of competitive compounds, $\Delta\mu_i$ (i=Zn, O, Er, or N) must also satisfy the other four conditions: $\Delta\mu_{Zn}+\Delta\mu_O\leq\Delta H_f(\mathrm{ZnO})$, $2\Delta\mu_{Er}+3\Delta\mu_O\leq\Delta H_f(\mathrm{Er_2O_3})$, $3\Delta\mu_{Zn}+2\Delta\mu_N\leq\Delta H_f(\mathrm{Zn_3N_2})$, and $\Delta\mu_{Er}+\Delta\mu_N\leq\Delta H_f(\mathrm{ErN})$. The formation enthalpies of ZnO, Er_2O_3, Zn_3N_2 and ErN have been calculated and the results are $\Delta H_f(\mathrm{ZnO})$=-3.342 eV, $\Delta H_f(\mathrm{Er_2O_3})$=-16.362 eV, $\Delta H_f(\mathrm{Zn_3N_2})$=-13.479 eV and $\Delta H_f(\mathrm{ErN})$=-13.131 eV, respectively. Since ZnO is used as the substrate material here, $-3.342\leq\Delta\mu_{Zn}\leq 0$ eV and $-3.342\leq\Delta\mu_O\leq 0$ eV must be satisfied firstly [see Figure S2(a)]. At the same time, due to Er and N as the doping material, $\Delta\mu_{Er}$ and $\Delta\mu_N$ are bound by them [see Figure S2(b), (c) and (d)]. The relative chemical potentials for $\Delta\mu_{Zn}$, $\Delta\mu_{Er}$, $\Delta\mu_N$, and $\Delta\mu_O$ according to their relationships, are shown in Figure S2. Four extreme conditions can be concluded from $\Delta\mu_{Zn}$, $\Delta\mu_{Er}$ and $\Delta\mu_N$ by the constraint of $\Delta\mu_O$, as displayed in Table S1 in the Supplementary Information.

3. VBM, CBM and *E*g

Table S2. VBM, CBM and E_g of the ZnO:(Er_{Zn}-mN_O) (m=0, 1, 2, 3, 4) doping systems

Defect	Er (at.%)	N (at.%)	VBM (eV)	CBM (eV)	E_g (eV)
Er_{Zn}	1.389	0	-0.225	3.056	3.281
Er_{Zn}-N_O	1.389	1.389	-2.157	1.275	3.432
Er_{Zn}-$2N_O$	1.389	2.778	-1.379	2.090	3.470
Er_{Zn}-$3N_O$	1.389	4.167	-1.493	2.015	3.507
Er_{Zn}-$4N_O$	1.389	5.556	-1.121	2.444	3.565

4. Electronic Density of States

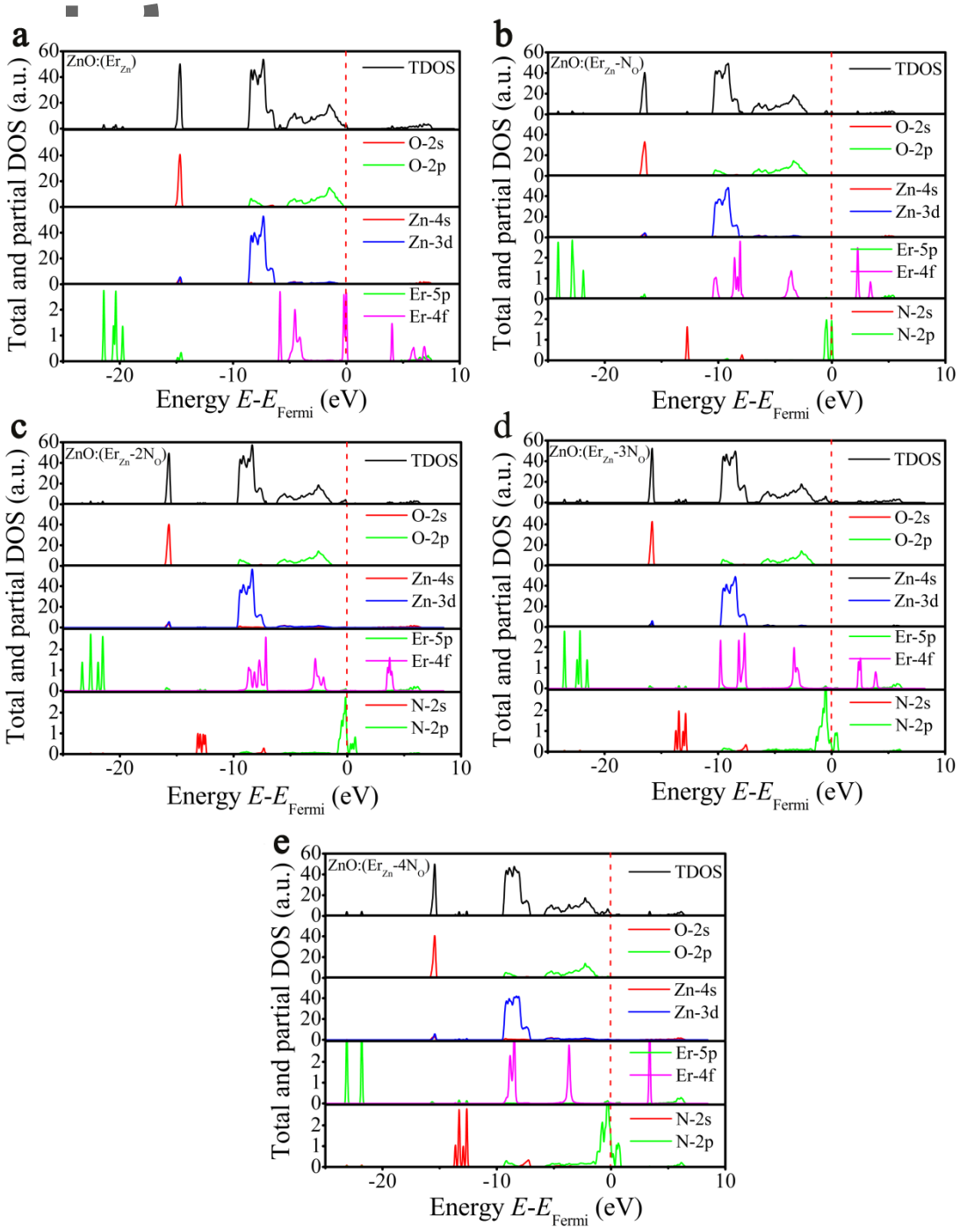

Figure S3. Density of electronic state. Total DOS (TDOS) and partial DOS (PDOS) of ZnO:(Er$_{Zn}$-mN$_O$) (m=0, 1, 2, 3, 4) calculated by GGA+U method. The Fermi level is set to

zero. After doping N into the ZnO:(Er_{Zn}) matrix, the Er-4*f* states move to lower energy. With further increasing the N concentration, the hybridization between N-2*p* and Zn-3*d* states and the localization of Er-4*f* states are gradually enhanced, but the hybridization between Er-4*f* and Zn-3*d* states weakens.

The distribution of the total and partial density of states (DOS) of electrons in the ZnO:(Er_{Zn}-mN_O) (*m*=0, 1, 2, 3, 4) systems were calculated and shown in Figure S3, in which the Fermi level is set to zero. From Figure S3(a), it can be seen that the valence band is composed of the hybridization among the Zn-3*d*, O-2*p* and Er-4*f* states, and the VBM is mainly attributed to the O-2*p* states. The conduction band is hybridized by the Zn-4*s*, Er-5*p* and Er-4*f* states, and dominated by Zn-4*s* states. After doping N into the ZnO:(Er_{Zn}) matrix, as shown in Figure S3(b), the Er-4*f* states move to lower energy. The resonance bonding effect of the Zn-3*d* states may weaken the hybridiztion between the O-2*p* and Zn-3*d* states, thus leading the valence band toward the lower energy. On the other hand, the shift of Zn-4*s*, Er-5*p* and Er-4*f* states to the lower energy leads to the downward shift of the CBM. In addition, it can be seen that the impurity band introduced by doping N is originated by the N-2*p* states. With further increasing the N concentration, as shown Figures S3(c), (d) and (e), the hybridization between N-2*p* and Zn-3*d* states and the localization of Er-4*f* states are gradually enhanced, but the hybridization between Er-4*f* and Zn-3*d* states weakens, which may be the reason for the VBM moving to higher energy.

5. First Brillouin Zone

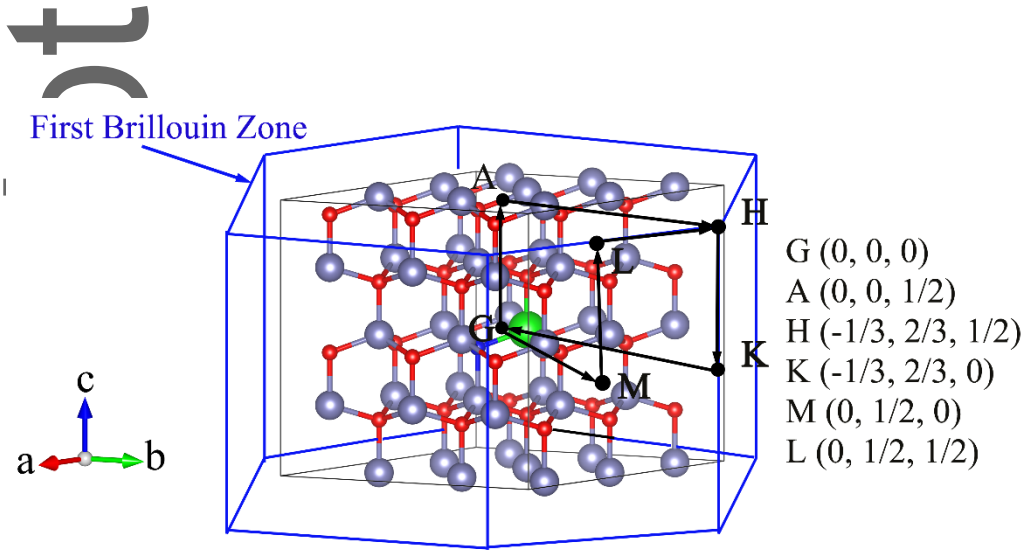

Figure S4. First Brillouin Zone. The G, A, H, K, M, and L points are marked out with coordinate values. They are Some special high symmetry points in the ZnO lattice.

6. Pair interactions

Table S3. Total energies of ZnO:(Er_{Zn}-N_O) with different Er_{Zn} and N_O distances.

Distance	1NN	2NN	3NN
Total energy (eV)	-80655.143	-80654.316	-80654.239

7. Optical properties

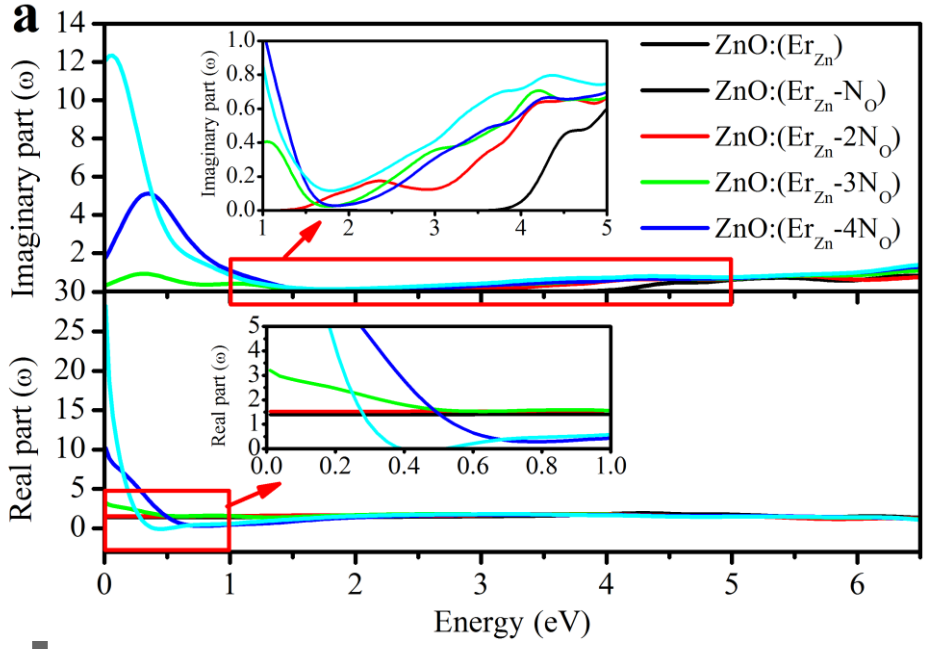

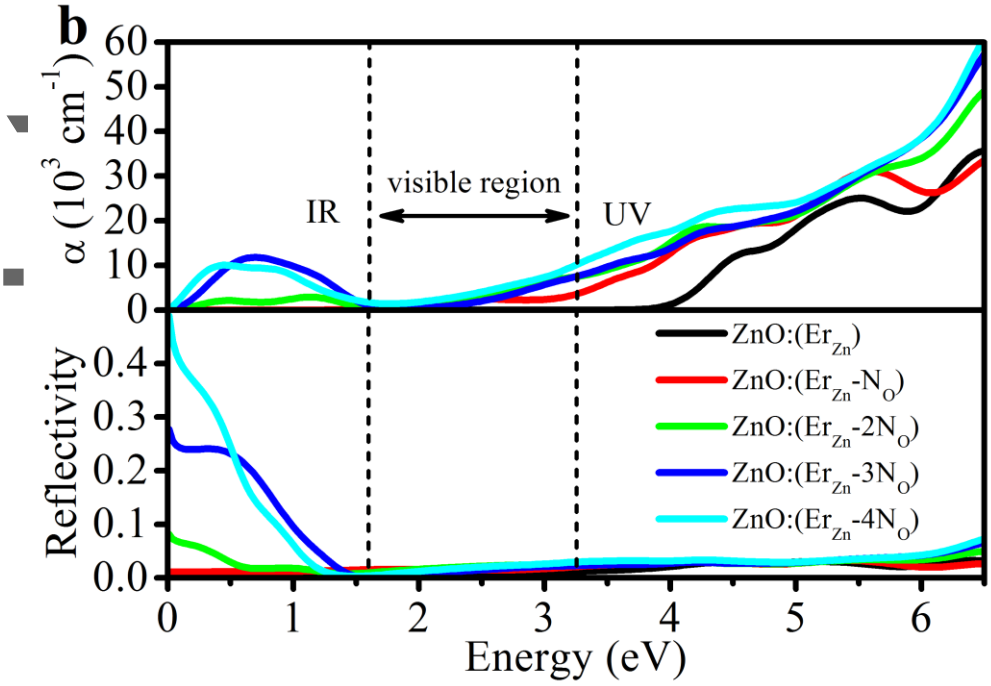

Figure S5. Optical properties. a The dielectric function of ZnO:(Er_{Zn}-mN_O) (m=0, 1, 2, 3, 4). **b** The absorption and reflectivity of ZnO:(Er_{Zn}-mN_O) (m=0, 1, 2, 3, 4). For m=2, 3, 4, there are three peaks in dielectric function curve, which originate from the transitions between the N-2*s* states and N-2*p* states, and their optical reflectivity is very high in the IR region. The optical absorption coefficient increases in both the visible and UV regions with the increasing incorporation of N atoms.

Figure S5(a) displays the dielectric function $\varepsilon(\omega)=\varepsilon_R(\omega)+i\varepsilon_i(\omega)$ of the ZnO:(Er_{Zn}-mN_O) (m=0, 1, 2, 3, 4) systems, where $\varepsilon_R(\omega)$ and $\varepsilon_i(\omega)$ are the real part and the imaginary part of the dielectric function, respectively. The imaginary part $\varepsilon_i(\omega)$ curve starts with an decreasing transition threshold with an increase in the N concentration, as 3.825, 1.466, 0, 0 and 0 eV for m=0, 1, 2, 3, and 4, respectively. For ZnO:(Er_{Zn}-mN_O) (m=2, 3, 4) systems, there are three

prominent peaks with an increasing peak intensity at 0.346, 0.346, and 0.066 eV, respectively, which originate from the transitions between the N-2*s* states and N-2*p* states. This phenomenon may be attributed to the boosted transition probability as the N concentration is increased. From the real part $\varepsilon_R(\omega)$ curve shown in Figure S5(a) and the lower inset, one can see that only the curve of ZnO:(Er_{Zn}-$4N_O$) possesses two energies with $\varepsilon_R(\omega)=0$ (0.384 eV and 0.542 eV, respectively, see the lower inset). For $\varepsilon_R(\omega)<0$ in the interval of 0.384~0.542 eV, the ZnO:(Er_{Zn}-$4N_O$) semiconductor exhibits metallic properties.

The optical absorption spectra of the ZnO:(Er_{Zn}-mN_O) (m=0, 1, 2, 3, 4) systems are predicted in Figure S5(b). The absorption edges redshift to lower energy with the increase of N concentration. This phenomenon is mainly due to the impurity band structures introduced by doping the N atoms (see Figure 3). The optical absorption coefficient increases in both the visible (1.5~3.2 eV) and ultraviolet (UV) regions with the increasing incorporation of N atoms. Moreover, the ZnO:(Er_{Zn}-mN_O) (m=2, 3, 4) systems also show considerable optical absorption in the infrared (IR) region when the concentration of N is above 1.389%. The corresponding reflectance spectra of the ZnO:(Er_{Zn}-mN_O) (m=0, 1, 2, 3, 4) systems are illustrated in Figure S5(b). The optical reflectivity of the ZnO:(Er_{Zn}-mN_O) (m=2, 3, 4) systems is very high in the IR region, which indicates that the transmittance of IR light is very low and the optical penetration of IR light will be poor for the considered materials. The optical absorption coefficient and reflectivity are both not high in the visible region for all the ZnO:(Er_{Zn}-mN_O) systems, which suggests that the transparency and penetration of the ZnO:(Er_{Zn}) film is little affected by doping N atoms.

8. P-type doping ZnO

Table S4. The doping elements for p-type doping ZnO.

Doping element	Valent state	Ionic radius	Refs.
Ag	1	100	S2
As	-3	222	S3

Au	1	137	S4
Be	2	31	S5
Bi	3	96	S6
C	-4	260	S7
Ce	3	103	S8
Co	3	74	S9
Cu	1	60	S10
Cs	1	169	S11
Fe	2	76	S12
K	1	133	S13
La	3	106	S14
Li	1	68	S15
Mg	2	65	S16
N	-3	171	S7
Na	1	95	S13
Nd	3	106	S17
Ni	2	72	S18
P	-3	212	S19
Sb	3	91	S20
Te	-2	221	S21
Y	3	83	S17
Yb	3	96	S17

Table S5. The codoping elements for p-type doping ZnO.

Doping element A	Doping element B	Valent state (A)	Ionic radius (A)	Refs.
Ag	N	2	97	S22
Al	N	3	50	S23
Al	P	3	50	S24
Al	C	3	50	S25
Al	As	3	50	S26
As	N	-3	222	S27
B	N	3	20	S28
Be	N	2	31	S29
C	N	-4	260	S30
Cr	C	3	64	S31
Cr	N	3	64	S32
Cu	Al	1	60	S33
Cu	N	1	60	S34
Er	K	3	88	S35
F	Li	-1	136	S36
Ga	N	3	62	S37
Ga	C	3	62	S25
Ga	P	3	62	S38
H	Li	1	10	S39

In	N	3	62	S37
In	Sb	3	62	S40
In	C	3	62	S25
Co	Li	2	74	S41
Li	P	1	68	S42
Mg	F	2	65	S43
Mg	N	2	65	S44
N	Li	-3	171	S45
N	P	-3	171	S46
Na	H	1	95	S47
Na	F	1	95	S48
P	N	-3	212	S49
S	N	-2	184	S50
S	Ag	-2	184	S51
Sb	N	3	91	S52
Sc	C	3	81	S32
Sn	N	2	102	S53
Te	N	6	56	S54
Ti	C	2	76	S31
V	N	3	74	S32
Zr	N	4	79	S26

References

[S1] H. Li, Y. Lv, J. Li, Y. Ke, *J. Alloys Comp.* **2014**, *617*, 102-107.

[S2] R. Kandulna, R. B. Choudhary, P. Maji, *J. Inorg. Org. Poly. Mater.* **2017**, *27*, 1760-1769.

[S3] T. H. Feng, X. C. Xia, *Opt. Mater. Expr.* 2017, *7*, 1281-1288.

[S4] Y. Xu, B. Yao, Y. F. Li, Z. H. Ding, J. C. Li, H. Z. Wang, Z. Z. Zhang, L. G. Zhang, H. F. Zhao, D. Z. Shen, *J. Alloys Compds.* **2014**, *585*, 479-484.

[S5] M. Chen, Y. Zhu, A. Chen, Z. Shen, Z. Tang, *Mater. Res. Bull.* **2016**, *78*, 16-19.

[S6] B. K. Singh, S. Tripathi, *J. Mater. Sci. Mater. Electr.* **2016**, *27*, 2360-2366.

[S7] W. Yu, J. Zhang, T. Peng, *Appl. Cataly. B Envir.* **2016**, *181*, 220-227.

[S8] Y. J. Liu, H. D. Zhang, X. Yan, A. J. Zhao, Z. G. Zhang, W. Y. Si, M. G. Gong, J. C. Zhang, Y. Z. Long, *RSC Adv.* **2016**, *6*. 85727-85734.

[S9] B. Henne, V. Ney, J. Lumetzberger, K. Ollefs, F. Wilhelm, A. Rogalev, A. Ney, *Phys. Rev. B* **2017**, *95*, 054406.

[S10] P. J. M. Isherwood, *Vacuum* **2017**, *139,* 173-177.

[S11] V. Ragupathi, S. Krishnaswamy, S. Sada, G. S. Nagarajan, S. Raman, *J. Mater. Sci.* **2014**, *49*, 7418-7424.

[S12] W. Zhao, X. Xiong, Y. Han, L. Wen, Z. Zou, S. Luo, H. Li, J. Su, T. Zhai, Y. Gao, Adv. Opti. Mater. **2017**, *5*, 1700146.

[S13] W. C. Au, K. Y. Chan, *Appl. Phys. A Mater. Sci. Proc.* **2017**, *123*. 485.

[S14] H. D. Zhang, M. Yu, J. C. Zhang, C. H. Sheng, X. Yan, W. P. Han, Y. C. Liu, S. Chen, G. Z. Shen, Y. Z. Long, *Nanoscale* **2015**, *7*, 10513-10518.

[S15] A. Igityan, N. Aghamalyan, S. Petrosyan, G. Badalyan, Y. Kafadaryan, *Phys. Stat. Solidi A Appl. Mater. Sci.* **2017**, *215*, 1700353.

[S16] H. Fang, J. Juang, S. Liu, *Inter. J. Nanotech.* **2017***, 14*, 992-1000.

[S17] B. Huang, *Phys. Chem. Chem. Phys.* **2017**, *19,* 12683-12711.

[S18] J. Qu, Y. Ge, B. Zu, Y. Li, X. Dou, *Small* **2016**, *12*, 1369-1377.

[S19] P. Sharma, G. Aaryashree, Vivek, S. Mukherjee, *J. Appl. Phys.* **2017**, *121*, 225306.

[S20] G. He, M. Jiang, B. Li, Z. Zhang, H. Zhao, C. Shan, D. Shen, *J. Mater. Chem. C* **2017**, *5,* 10938-10946.

[S21] Z. Yao, K. Tang, Z. Xua, J. Ma, J. Yea, S. Zhua, S. Gu, *J. Alloys Compds.* **2018**, *735*, 1232-1238.
[S22] Z. Xu, Q. Hou, L. Qu, *Inter. J. Modern Phys. B* **2017**, *31*, 1750008.
[S23] A. Ievtushenko, O. Khyzhun, I. Shtepliuk, O. Bykov, R. Jakieła, S. Tkach, E. Kuzmenko, V. Baturin, O. Karpenko, O. Olifan, *J. Alloys Compds.* **2017**, *722*, 683-689.
[S24] S. Shin, C. Kim, J. A. Lee, Y. W. Heo, J. H. Lee, J. J. Kim, *Ceram. Inter.* **2017**, *43*, 11163-11169.
[S25] H. Li, Y. Lv, H. Fu, J. Li, K. Yu, *J. Appl. Phys.* **2015**, *117*, 055701.
[S26] L. Balakrishnan, S. Gowrishankar, J. Elanchezhiyan, N. Gopalakrishnan, *Physica B* **2011**, *406*, 4447-4452.
[S27] E. Przezdziecka, E. Kaminska, K. P. Korona, E. Dynowska, W. Dobrowolski, R. Jakiela, L. Klopotowski, J. Kossut, *Sci. Tech.* **2007**, *22*, 10.
[S28] X. Chen, Z. Zhang, B. Yao, Y. Zhang, Y. Gu, P. Zhao, B. Li, D. Shen, *J. Alloys Compds.* **2016**, *672*, 260-264.
[S29] A. Chen, H. Zhu, Y. Wu, M. Chen, Y. Zhu, X. Gui, Z. Tang, *Adv. Func. Mater.* **2016**, *26*, 3696-3702.
[S30] P. Liang, C. Zhang, H. Sun, S. Liu, M. Tadé, S. Wang, *RSC Adv.* **2016**, *6*, 85727-85734.
[S31] P. J, W. S, C. Q, H. J, W. J, *Chem. Phys. Chem.* **2014**, *15*, 1611-1618.
[S32] J. Zhang, K. Tse, M. Wong, Y. Zhang, J. Zhu, *Front. Phys.* **2016**, *11*, 117405. [S33] Y. Y. Bu, *Ceram. Inter.* **2015**, *41*, 4042-4049.
[S34] W. Ling, Z. WeiFeng, *Chin. Phys. Lett.* **2013**, *30*, 87203.
[S35] D. E. Aimouch, S. Meskine, A. Bahnes, A. Boukortt, A. Zaoui, *Optik* **2017**, *144* 539-545.
[S36] L. Cao, L. Zhu, Y. Li, M. Yang, Z. Ye, *Mater. Lett.* **2012**, *86*, 34-37.
[S37] L. Honglin, L. Yingbo, L. Jinzhu, Y. Ke, *Phys. Scripta* **2015**, *90*, 025803.
[S38] W. S. Noh, J. A. Lee, J. H. Lee, Y. W. Heo, J. J. Kim, *Ceram. Inter.* **2016**, *42*, 4136-4142.
[S39] F. Xiu, J. Xu, P. C. Joshi, C. A. Bridges, M. P. Paranthaman, *Springer* **2016**, *218*, 105-140.
[S40] M. Türker, M. Deicher, K. Johnston, H. Wolf, T. Wichert, *Hyperfine Interact.* **2015**, *231*, 65-71.
[S41] S. Ullah Awan, S. K. Hasanain, G. Hassnain Jaffari, Z. Mehmood, *Appl. Phys. Lett.* **2014**, *104*, 222906.

[S42] P. Sharma, R. Bhardwaj, R. Singh, S. Kumar, S. Mukherjee, *Appl. Phys. Lett.* **2017**, *111*, 091604.
[S43] G. Muruganandam, N. Mala, S. Pandiarajan, N. Srinivasan, R. Ramya, E. Sindhuja, K. Ravichandran, *J. Mater. Sci. Mater. Electr.* **2017**, *28*, 18228-18235.
[S44] L. Chen, Z. Xiong, Q. Wan, D. Li, *Opt. Mater.* **2010**, *32*, 1216-1222.
[S45] Y. Gai, G. Tang, J. Li, *J. Phys. Chem. Solids* **2011**, *72*, 725-729.
[S46] Y. R. Sui, B. Yao, L. Xiao, L. L. Yang, J. Cao, X. F. Li, G. Z. Xing, J. H. Lang, X. Y. Li, S. Q. Lv, *Appl. Surf. Sci.* **2013**, *287*, 484-489.
[S47] J. Li, Y. Liu, Z. Mei, L. Vines, A. Kuznetsov, X. Du, *Mater. Sci. Semiconduct. Proc.* **2017**, *69*, 28-31.
[S48] S. Deng, Z. Jiang, *Acta Phys. Sinica* **2014**, *63*, 077101.
[S49] Y. R. Sui, B. Yao, L. Xiao, L. L. Yang, J. Cao, X. F. Li, G. Z. Xing, J. H. Lang, X. Y. Li, S. Q. Lv, *Appl. Surf. Sci.* **2013**, *287*, 484-489.
[S50] W. Niu, H. Xu, Y. Guo, Y. Li, Z. Ye, L. Zhu, *Phys. Chem. Chem. Phys.* **2015**, *17*, 16705-16708.
[S51] N. X. Tian, L. Xiang, L. Zhong, Y. C. Yong, H. S. Cheng, Z. W. Hui, *Appl. Surf. Sci.* **2014**, *316*, 62-65.
[S52] T. Guo, G. Dong, Q. Chen, X. Diao, F. Gao, J. Phys. Chem. Solids **2014**, *75*, 42-47.
[S53] N. Nripasree, N. K. Deepak, *Mater. Sci. Eng. B Adv. Func. Solid State Mater.* **2016**, *211*, 121-127.
[S54] K. Tang, S. Zhu, Z. Xu, Y. Shen, J. Ye, S. Gu, *J. Alloys Compds.* **2017**, *699*, 484-488.

Methods

All calculations are carried out by the CASTEP code package [S55] based on density functional theory. It is widely used in the field of chemistry and materials science. By simulation calculation, we can get the crystal structures, formation energies, ionization energies, band structures and optical properties. It is good to predict the physical properties of the materials and provide a good way for material engineering design. The First Brillouin Zone of ZnO lattice model, and some special high symmetry points in the lattice are illustrated in Figure S4 in Supplement Information, marked out with coordinate values as G, A, H, K, M and L, respectively.

The Model of the codopants system

A 3×3×2 supercell containing 72 atoms were used for all the models in this paper. To evaluate the stability of the crystal structures, the ZnO supercell was firstly doped with one Er atom (Er_{Zn}, Er atom occupying the site of Zn atom) and one N (N_O, N atom occupying the site of O atom), in which the distances between Er_{Zn} and N_O was set as the nearest-neighbor (1NN), the second nearest-neighbor (2NN) and the third nearest-neighbor (3NN), respectively. Relaxation calculations of these ZnO:(Er_{Zn}-N_O) models were then carried out by varying the distances between the Er_{Zn} and N_O atoms. Table S2 in Supplementary Information shows the total energies of the ZnO:(Er_{Zn}-N_O) models, from which one can find that the total energy decreases slightly when the distance is decreased from 3NN to 1NN. The total energy is the lowest when the distance is located at 1NN, indicating that the Er-N codoped ZnO is most stable at 1NN position. Therefore, Er-N codoped ZnO at 1NN position is used for the dopants in the following of this work.

For the codoped systems, different Er and N concentrations play important roles on the stability of the models. In order to obtain representative codoping systems effectively in our study, some special models of ZnO:(Er_{Zn}), ZnO:(N_O), ZnO:($2Er_{Zn}$), ZnO:(Er_{Zn}-N_O), ZnO:($2N_O$), ZnO:($3Er_{Zn}$), ZnO:($2Er_{Zn}$-N_O), ZnO:(Er_{Zn}-$2N_O$), ZnO:($3Er_{Zn}$-N_O), ZnO:($2Er_{Zn}$-$2N_O$), ZnO:(Er_{Zn}-$3N_O$), ZnO:($4Er_{Zn}$-N_O), ZnO:($3Er_{Zn}$-$2N_O$), ZnO:($2Er_{Zn}$-$3N_O$), and ZnO:(Er_{Zn}-$4N_O$) were constructed and their formation enthalpies were calculated. The results are shown in Figure 1(b). It is obvious that the formation enthalpies vary linearly with the concentration of N for the complexes with same number of total dopants. So two representative codoping complexes [ZnO:(Er_{Zn}-mN_O) (m=0, 1, 2, 3, 4) and ZnO:(nEr_{Zn}-N_O) (n=0, 1, 2, 3, 4)] were proposed and studied to evaluate the structural, electronic, and optical properties of the Er-N codoping in ZnO in this work. ZnO:(Er_{Zn}-mN_O) (m=0, 1, 2, 3, 4) [ZnO:(nEr_{Zn}-N_O) (n=0, 1, 2, 3, 4)] corresponds to concentration of the N (Er) dopants of 0 at.%, 1.389 at.%, 2.778 at.%, 4.167 at.% and 5.556 at.% for different m (n), respectively. Figure 1(a) shows partial view of the models considered in this work.

Defect formation energies and ionization energies

Defect formation energy of each system is defined by the formula as follows:

$$\Delta E_f(\alpha,q) = E_t(\alpha,q) - E_t(\mathrm{ZnO}) - \sum_i n_i(\mu_i + \Delta\mu_i) + q[E_{Fermi} + E_{VBM}(\mathrm{ZnO}) + \Delta V] \quad (1)$$

where $E_t(\alpha, q)$ is the total energy of the system containing defect α and charge q, and E_t(ZnO) is the total energy of the intrinsic ZnO bulk material. n_i is the atom number of element i (i = Zn, Er, O or N) that is added to ($n_i > 0$) or removed from ($n_i < 0$) the intrinsic ZnO bulk material. μ_i is the chemical potential of element i. $\Delta\mu_i$ is the relative chemical potential of element i which is determined by the relationship as follows: $\Delta\mu_i$=μ_i(compound)–μ_i(elementary substance). E_{Fermi} is the Fermi level of the system with its value varying between valence band maximum (VBM) and conduction band minimum (CBM), namely the bandgap (E_g). E_{VBM}(ZnO) is the VBM energy of the intrinsic ZnO. ΔV is the correction potential introduced to describe the electrostatic potential difference between the supercells with and without a dopant impurity.

In the first-principles calculations, ionization energy $\varepsilon(q/q')$ of a semiconductor material can be described by Eq. (2) and defined as the Fermi energy [E_{Fermi} in Eq. (1)] when the defect formation energy $\Delta E_f(\alpha, q)$ of the system with a defect α and charge q is equal to that of the defect α but with another charge q'. From Eq. (2), it is obvious that the ionization energy $\varepsilon(q/q')$ is independent on the chemical potential μ_i of each element i.

$$\varepsilon(q/q') = \frac{E_t(\alpha,q) - E_t(\alpha,q') + q\Delta V - q'\Delta V'}{q' - q} - E_{VBM}(\mathrm{ZnO}) \quad (2)$$

Chemical potentials

From the Eq. (1), it can be seen that the defect formation energy $\Delta E_f(\alpha, q)$ is closely related with the μ_i and $\Delta\mu_i$ of each element i, of which μ_i and $\Delta\mu_i$ also need to be determined. Under specific thermodynamic equilibrium conditions, μ_i and $\Delta\mu_i$ are both limited by the growth conditions. The value of μ_{i} is determined by total energy of gas or solid formed by element i. Specifically, μ_{Zn}=E_t(Zn), μ_{Er}=E_t(Er), μ_O=1/2E_t(O_2), μ_N=1/2E_t(N_2), where E_t(Zn) and E_t(Er) are the total energies of Zn and Er solids, respectively, and E_t(O_2) and E_t(N_2) are the total energies of oxygen and nitrogen molecules placed in the 15×15×15 Å^3 cube, respectively. $\Delta\mu_{\mathrm{i}}$

is the relative chemical potential of element i in a particular environment, and can be calculated by the formula: $\Delta\mu_i=\mu_i$(compound)-μ_i, where μ_i(compound) is the chemical potential of element i in a specific compound. However, the value of $\Delta\mu_i$ cannot be gained directly because μ_i(compound) cannot be calculated directly. But $\Delta\mu_i$ can be obtained to be limited in a particular range by the constraints of formation enthalpies and bulk thermodynamic equilibrium conditions.

References

[S55] M. D. Segall, P. J. D. Lindan, M. J. Probert, C. J. Pickard, P. J. Hasnip, S. J. Clark, M. C. Payne, *J. Phys.: Condens. Matter* **2002**, *14*, 2717–2744 .

Data availability

The datasets generated during and/or analyzed during the current study are available from the corresponding author on reasonable request.